

Giant spin-splitting and gap renormalization driven by trions in single-layer $\text{WS}_2/\text{h-BN}$ heterostructures

Jyoti Katoch^{*,1} Søren Ulstrup^{*,2,3} Roland J. Koch,² Simon Moser,² Kathleen
M. McCreary,⁴ Simranjeet Singh,¹ Jinsong Xu,¹ Berend T. Jonker,⁴ Roland
K. Kawakami,¹ Aaron Bostwick,² Eli Rotenberg,² and Chris Jozwiak^{†2,5}

¹ *Department of Physics, The Ohio State University, Columbus, Ohio 43210, USA*

² *Advanced Light Source, E. O. Lawrence Berkeley
National Laboratory, Berkeley, California 94720, USA*

³*Department of Physics and Astronomy,
Interdisciplinary Nanoscience Center (iNANO),
Aarhus University, 8000 Aarhus C, Denmark*

⁴*Naval Research laboratory, Washington, D.C. 20375, USA*

⁵ * *These authors contributed equally to the work.*

[†] *Email: CMJozwiak@lbl.gov*

In two-dimensional (2D) semiconducting transition metal dichalcogenides (TMDs), new electronic phenomena such as tunable band gaps [1–3] and strongly bound excitons and trions emerge from strong many-body effects [4–6], beyond spin-orbit coupling- and lattice symmetry-induced spin and valley degrees of freedom [7]. Combining single-layer (SL) TMDs with other 2D materials in van der Waals heterostructures offers an intriguing means of controlling the electronic properties through these many-body effects via engineered interlayer interactions [8–10]. Here, we employ micro-focused angle-resolved photoemission spectroscopy (microARPES) and *in-situ* surface doping to manipulate the electronic structure of SL WS₂ on hexagonal boron nitride (WS₂/h-BN). Upon electron doping, we observe an unexpected giant renormalization of the SL WS₂ valence band (VB) spin-orbit splitting from 430 meV to 660 meV, together with a band gap reduction of at least 325 meV, attributed to the formation of trionic quasiparticles. These findings suggest that the electronic, spintronic and excitonic properties are widely tunable in 2D TMD/h-BN heterostructures, as these are intimately linked to the quasiparticle dynamics of the materials [11–13].

Coulomb interactions in 2D materials are several times stronger than in their 3D counterparts. In 2D TMDs, this is most directly evidenced by the presence of excitons with an order of magnitude higher binding energies than in the bulk [4]. While the excitons in these 2D materials have been widely studied by optical techniques [13], the impact of strong electron-electron interactions on the quasiparticle band structure remains unclear. Theory predicts many-body effects to influence the spin-orbit splitting around the valence band maximum (VBM) and conduction band minimum (CBM) [14]. While these should be observable by ARPES, a direct probe of many-body effects [15], measurements so far have mainly focused on the layer-dependence of the single-particle spectrum and the direct band gap transition in 2D TMD systems, including epitaxial SL MoSe₂ [16] and SL WSe₂ [17] grown on doped multilayer graphene, and SL MoS₂ grown on a metal surface [18]. On such conductive substrates the interfacial interactions and screening are known to strongly influence the electronic properties of the SL TMD [9].

Flakes of SL TMDs have been transferred on oxide substrates such as SiO₂ where the substrate screening and interfacial effects are potentially reduced. However, resulting ARPES spectra have been too broad for detailed analysis [19], likely due to large surface roughness

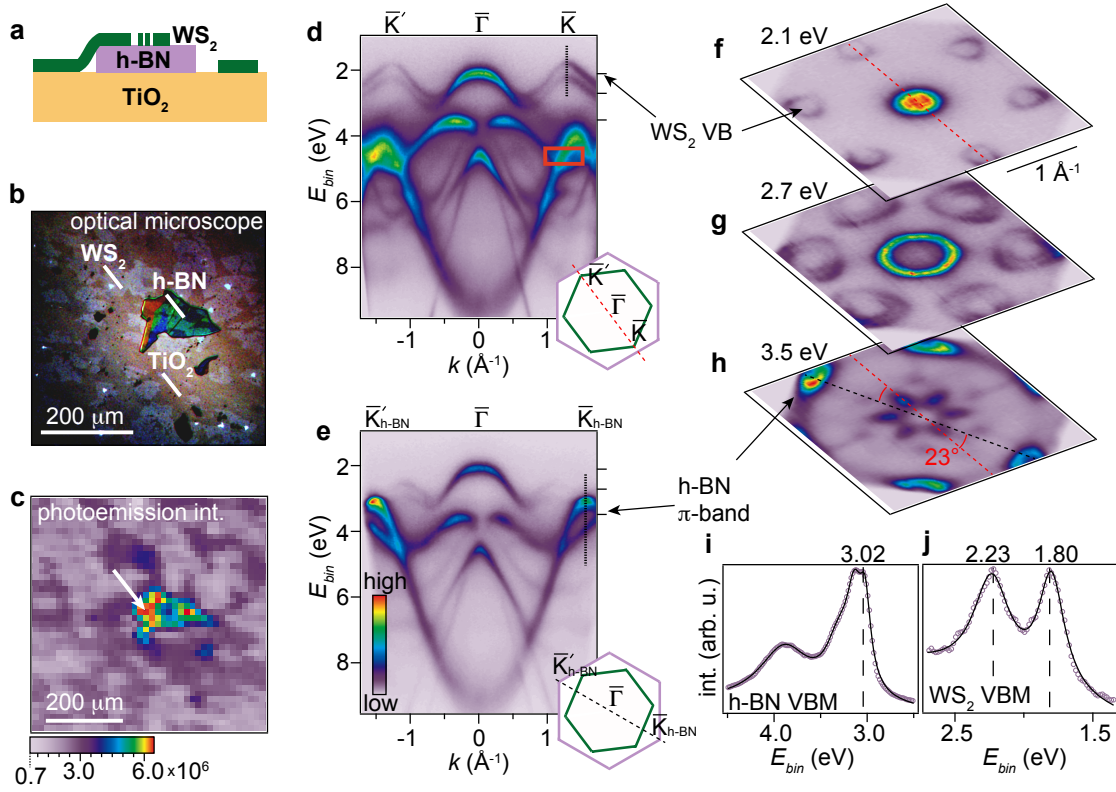


FIG. 1: **Spatially-resolved electronic structure mapping of a $\text{WS}_2/\text{h-BN}$ heterostructure supported on TiO_2 .** **a**, Side-view sketch of $\text{WS}_2/\text{h-BN}$ on TiO_2 , illustrating SL WS_2 regions contacted directly to h-BN and to TiO_2 . **b**, Optical microscope image of the sample. The contrast has been strongly enhanced to better visualize the SL WS_2 . Brown patches correspond to bare TiO_2 , light purple to WS_2/TiO_2 and the darker green/red structure is the h-BN flake. **c**, Spatial map of photoemission intensity (integrated over the red box in (d)) for the same region seen in **b**. See Supplementary Section 1 for details on the spatial intensity variations. **d**, Measured dispersion along the $\bar{K}'\text{-}\bar{\Gamma}\text{-}\bar{K}$ direction of the SL WS_2 BZ (see green BZ and dashed red line in the insert) collected at the spatial coordinates marked by a white arrow in **c**. The rectangular red box marks a region with crossing WS_2 and h-BN bands where the photoemission intensity is integrated to produce the spatial map in **c**. **e**, ARPES dispersion in the high symmetry direction of h-BN (see purple BZ and dashed black line in the insert). **f-h**, Constant energy cuts obtained at the given binding energies (see also ticks on the right of panels **d-e**). Arrows mark distinct energy contours relating to SL WS_2 and to h-BN. The red and black dashed lines (insert in **d-e**) indicate a twist angle of $(23 \pm 1)^\circ$ in between the SL WS_2 and h-BN. **i-j**, EDCs obtained along the dotted lines in **d-e** around the h-BN VBM (**i**) and SL WS_2 VBM (**j**). The positions of the band edges are given in units of eV and the error bar is 30 meV. 3

and charge impurity scattering [20]. With respect to SiO_2 and similar substrates, h-BN has favorable qualities like atomic flatness, modest screening and a homogeneous charge distribution. This should enable direct investigation of the adjacent TMD's intrinsic electronic structure and many-body effects. h-BN is often used as a substrate for graphene heterostructures [8, 20] with high device performance [21] and new exotic electronic states such as quantized Dirac cones [22]. Unfortunately, the lateral size of mechanically assembled heterostructures is usually on the order of $\sim 10 \mu\text{m}$, much smaller than the beam spot of typical ARPES setups ($\gtrsim 100 \mu\text{m}$). Furthermore, sample charging on insulating bulk h-BN substrates would complicate ARPES experiments.

We overcome these challenges as follows. We realize a high quality 2D semiconductor-insulator interface by mechanical transfer of a relatively large ($\sim 100 \mu\text{m}$) SL WS_2 crystal over a thin flake of h-BN that was transferred onto a degenerately doped TiO_2 substrate, as depicted in Fig. 1(a). Sample charging is avoided by electrically contacting the continuous SL WS_2 flake to both the h-BN and the conductive TiO_2 . Fig. 1(b) is an optical microscope image of the sample, including a $\approx 100 \mu\text{m}$ wide h-BN flake, surrounded by several transferred flakes of SL WS_2 on the TiO_2 substrate (WS_2/TiO_2), one of which partially overlaps the h-BN.

By using a state-of-the-art spatially-resolved microARPES experiment with a $10 \mu\text{m}$ focused synchrotron beam spot, we are able to collect distinct high quality band structure information from the multiple micron-scale interfaces. A spatial map of the photoemission intensity around the $\text{WS}_2/\text{h-BN}$ heterostructure is shown in Fig. 1(c), which was produced by integrating the intensity over the boxed region of the corresponding k -space band structure shown in Fig. 1(d), measured at each spatial point. The crossing SL WS_2 and h-BN bands in this region ensure strong contrast between $\text{WS}_2/\text{h-BN}$ (white arrow), regions of WS_2/TiO_2 (light purple), and regions of bare TiO_2 (dark purple) in the spatial map. The photoemission map (panel (c)) corresponds directly to the optical micrograph (panel (b)) with contrasts that reflect the intensity of the WS_2 and h-BN features in the red box in panel (d). The band structures from bare TiO_2 , WS_2/TiO_2 and several spots within the $\text{WS}_2/\text{h-BN}$ heterostructure are presented in Supplementary Figure S1. The slight intensity variations within the $\text{WS}_2/\text{h-BN}$ heterostructure arise from areas with pinholes introduced in the SL WS_2 during transfer, as sketched in Fig. 1(a) [23]. The sensitivity towards such features, which are not resolved by the optical micrograph, demonstrates the capability of

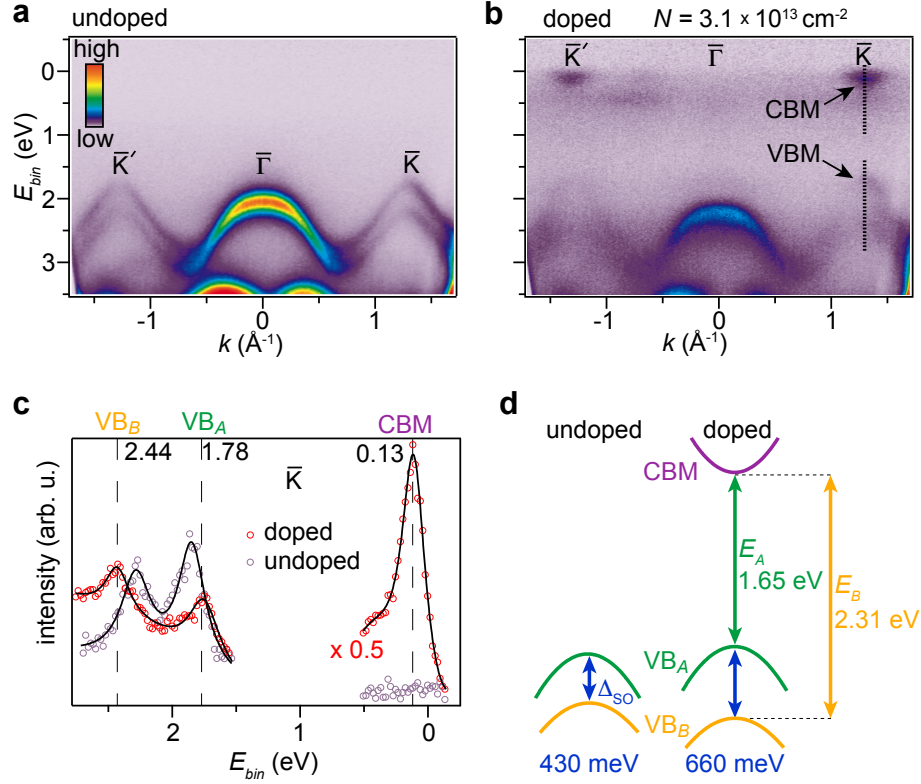


FIG. 2: Electronic structure of strongly electron-doped $\text{WS}_2/\text{h-BN}$. **a**, Dispersion of SL $\text{WS}_2/\text{h-BN}$ along the $\bar{K}-\bar{\Gamma}-\bar{K}'$ direction of the SL WS_2 BZ, collected from the spot marked by the white arrow in Fig. 1(c). **b**, Corresponding data at the highest achieved electron-doping N . **c**, EDCs (markers) around the VBM and CBM at \bar{K} (see dotted lines and arrows in **b**) for undoped and electron-doped SL WS_2 on h-BN. Peak positions extracted from Lorentzian line fits (curves) are shown as vertical dashed lines and values for the doped case are given in units of eV. Note that the CBM intensity has been scaled by a factor of 0.5 in order to make the comparison with the other peaks more clear. **d**, Schematics of the dispersion change of the VB spin-orbit split bands VB_A and VB_B due to doping and the measured energy gaps between the CBM and VB_A (denoted as E_A) and VB_B (denoted as E_B) in the doped case. The energy splitting due to spin-orbit coupling Δ_{SO} and the values of E_A and E_B are provided with error bars of 30 meV.

identifying optimum sample areas directly in the ARPES experiment, which is critical for such complex, heterogenous samples.

The VB electronic structure through the entire first Brillouin zone (BZ) of the het-

erstructure, including the SL WS₂ bands and the π -band dispersion of the underlying h-BN, is shown in Figs. 1(d)-(e). The data is collected from a single spatial point where the WS₂ features are most intense (white arrow in Fig. 1(c)). Custom electrostatic deflectors mounted in the photoelectron analyzer enable full scans of k -space at exactly this position without any drift from sample motion. The BZ orientations and twist angle between the two materials are determined from the constant binding energy cuts shown in Figs. 1(f)-(h). From the relative orientation of the hole pockets, we estimate a twist angle of $(23 \pm 1)^\circ$. The energy distribution curves (EDCs) in Fig. 1(i)-(j) track the VBM binding energy positions of the two materials. The upper VB of SL WS₂ is located inside the band gap of h-BN and the SL WS₂ VBM is characterized by a spin-orbit splitting of 430 meV (see Fig. 1(j)), in agreement with theoretical predictions [12] and previous experiments [23, 24]. The clear electronic states and lack of band hybridization reveal a weak interlayer interaction between the two materials. Similar to work on graphene/h-BN [22], we expect these data to represent the intrinsic electronic structure of SL WS₂ with negligible substrate influence.

The impact of electron doping on the electronic structure via *in-situ* surface potassium deposition is shown in Fig. 2(a,b) (see Supplementary Figure S2 for core level data on clean and potassium dosed samples). Doping WS₂/h-BN leads to the CBM being populated at the \bar{K} points of SL WS₂, confirming the expected direct band gap. A surprising change of the dispersion of the two spin-orbit split bands VB_A and VB_B of WS₂/h-BN around the \bar{K} point is observed, highlighted in the EDCs in Fig. 2(c). The spin-splitting due to spin-orbit coupling Δ_{SO} increases from 430 meV in the undoped case to 660 meV in the electron-doped case, as sketched in Fig. 2(d). Such a large spin-splitting has not previously been observed in any SL material to our knowledge. In this case, the band gap of SL WS₂ is 1.65 eV and the CBM to VB_B offset is 2.31 eV. These values are sketched in Fig. 2(d) and denoted as E_A and E_B , respectively, due to the relation with the A and B exciton lines observed in optical experiments [5].

A detailed evolution of the band extrema with increasing doping is shown in Fig. 3(a-e). The dispersions around the VBM as determined from EDC line shape analysis (see Supplementary Figure S6) are shown by dashed red curves and directly compared in panel (f). We estimate the charge carrier density, N , at each dosing step from the CBM position (see methods). These estimated doping levels are consistent with those achieved in similar experiments on bulk WSe₂ [25] and with the intensity of the potassium 3p core level (see

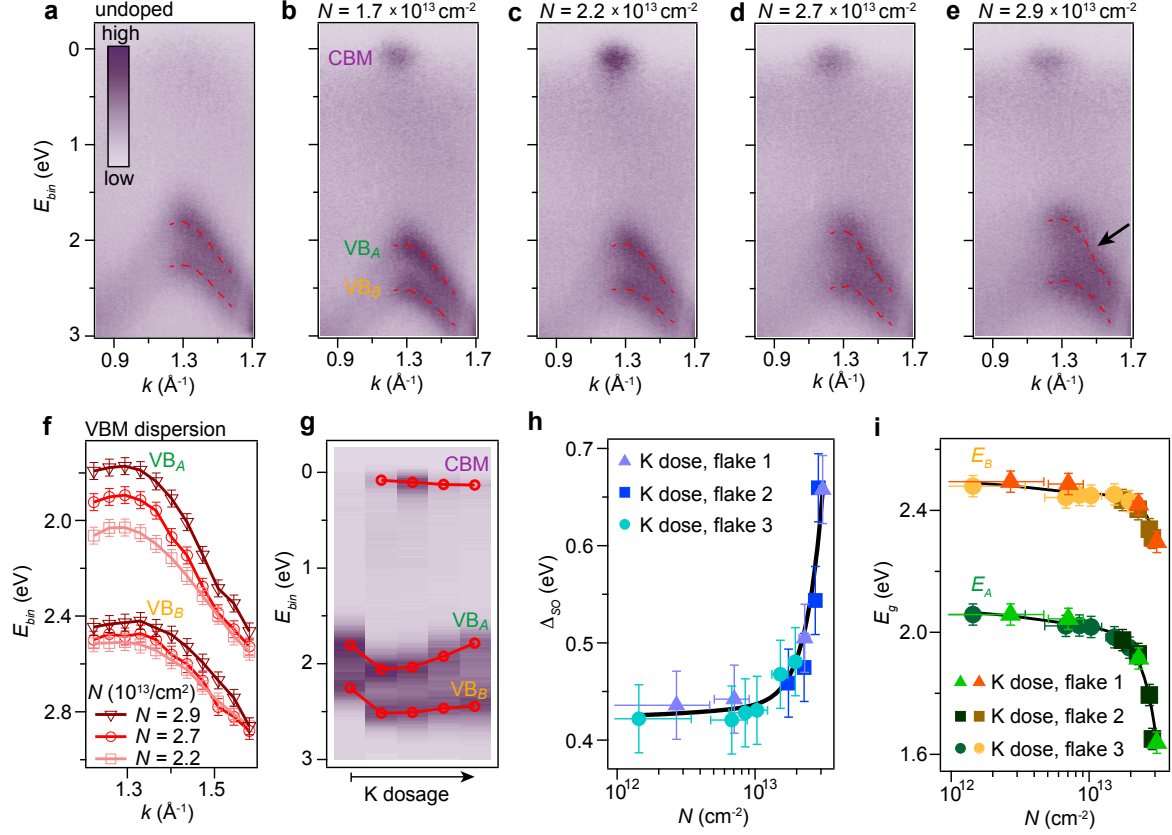


FIG. 3: Evolution of SL WS₂ VBM and CBM dispersion with charge carrier density. **a-e**, microARPES measurements around the \bar{K} -point of SL WS₂/h-BN for clean (**a**) and increasingly potassium-dosed cases (**b**)-(e). The red curves are the fitted VB_A and VB_B dispersions determined via double Lorentzian fits of EDCs (see Supplementary Figure S6). The arrow in **e** points to a possible kink in VB_A. **f**, VB_A and VB_B dispersions extracted from the EDC analysis in the strongly electron doped cases. **g**, ARPES intensity at the \bar{K} -point and peak positions (red markers) at each potassium dosing step (see corresponding EDC analysis in Supplementary Figure S7). **h-i**, Spin-orbit splitting (**h**) and band gap values (**i**) determined from the VB_A, VB_B and CBM positions, combining data from K doping experiments on the different WS₂/h-BN flakes investigated here, in Fig. 2 and in Supplementary Figure S8. The lines in **h-i** are provided as guides to the eye.

Supplementary Figure S3).

From EDC peak positions at \bar{K} (see Supplementary Figure S7), we extract the VBM and CBM energies as a function of dosing (panel (g)). After the first dosing step ($N = 1.7 \times 10^{13} \text{ cm}^{-2}$), the CBM becomes occupied and VB_A and VB_B rigidly shift to higher

binding energy. With further dosing, the CBM moves further down to higher binding energy, while VB_A and VB_B shift back towards lower binding energy, resulting in a continuous narrowing of the band gap. In particular, the dispersion of VB_A appears to renormalize with increased doping (see panels (d,e,f)), with a dramatic increase in Δ_{SO} (panels (g,h)). This leads to a corresponding change in the relative energy separation between E_A and E_B (panel (i)), implying that the energies of the A and B exciton lines also separate. The data points with different marker shape and color in panels (h,i) stem from separate doping experiments on the three different flakes studied in Fig. 2, Fig. 3 and in Supplementary Figure S8. A reproducible trend is found across all flakes. Note also that in the carrier density range between $2 \times 10^{12} \text{ cm}^{-2}$ and $1.0 \times 10^{13} \text{ cm}^{-2}$ we find a more modest band gap renormalization of $(90 \pm 30) \text{ meV}$, which is in excellent agreement with gated device measurements on a similar sample [1]. Our observations reveal that it is insufficient to only consider rigid band shifts, and that strong dispersion changes can result from doping of SL TMDs.

The surprising doping-induced changes in Δ_{SO} are likely not directly related to the surface potential induced by the potassium deposition (through, *e.g.*, the Rashba interaction) which is not expected to affect Δ_{SO} at \bar{K} for SL TMDs. This rather introduces a splitting at $\bar{\Gamma}$, which we do not observe [26, 27]. Furthermore, we can rule out any potassium induced structural symmetry breaking in our heterostructure, as only minor rigid binding energy shifts of the S 2p core levels of WS_2 and of the underlying h-BN π -band are observed after complete doping (see Supplementary Figures S4-S5). The reproducible charge carrier dependence of the spectral changes demonstrated in Figs. 2-3 and Supplementary Figure S8 suggest that these changes originate from Coulomb interactions around the band extrema of SL WS_2 [1, 2, 14].

The linewidths of the VB_A and CBM peaks exhibit a non-monotonic dependence with doping, which can not be described by simple scattering on ionized potassium impurities (see further discussion in Supplementary Section 4). Specifically, the observation that VB_A renormalization coincides with occupation of the CBM suggests that the renormalization is caused by new scattering channels available upon occupation of the conduction band (CB). Previous works utilizing surface potassium deposition for electron-doping of SL TMDs on conductive substrates [16–18] have shown no such changes in Δ_{SO} , where the Coulomb interactions are already strongly screened in the undoped case [9]. We believe that the

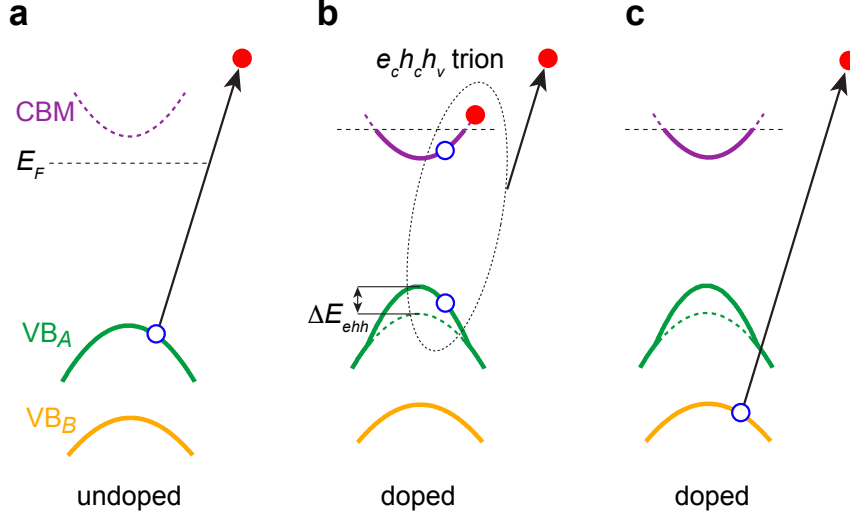


FIG. 4: **Quasiparticle dynamics in doped SL WS₂.** **a**, Band diagram illustrating the generated photohole (hollow blue circle) in VB_A and the photoemitted free electron (filled red circle) in the undoped situation. **b**, Illustration of an $e_c h_c h_v$ trionic quasiparticle generated in doped SL WS₂. The photohole binding energy is lowered and the VB_A dispersion renormalizes with respect to the bare band (green dashed curve) by the trion binding energy ΔE_{ehh} . **c**, A photohole generated in VB_B in the doped situation undergoes a process that is analogous to the undoped situation in **a** due to the absence of strong trion interactions with photoholes in this band.

reduced dielectric constant of the h-BN substrate plays a key role for these observations as it leads to reduced screening of the many-body interactions in the bare SL WS₂.

An alkali-atom-induced renormalization of the VB edge at K towards E_F , observed in several bulk TMDs, has been attributed to the breaking of the outermost layers' degeneracy by the doping-induced field [25, 28]. This can either be a single-particle effect [28] or a combination of single- and many-body effects [25], the latter of which suggests a negative electronic compressibility (NEC), the motion of the chemical potential μ towards the VBM, i.e. $d\mu/dN < 0$.

In contrast, we observe distinctive effects in SL WS₂/h-BN, namely 1) a renormalization of Δ_{SO} within the single layer, 2) an NEC in which $|d\mu/dN|$ is significantly larger than in the bulk [25, 28], and 3) the VB_A slope is discontinuous at $k = (\bar{K}, \bar{K}') \pm \sim 0.15 \text{ \AA}^{-1}$ in Fig. 2(b) at high doping. This leads to kinks in VB_A, exemplified by the arrow in Fig. 3(e), which develop continuously in strength with doping in Figs. 3(a)-(e). Such kinks are

common in ARPES when the created “photohole” interacts strongly with well-defined (in energy and/or momentum) excitations [15].

As noted above, the band renormalization coincides with the occupation of the CB, suggesting that such excitations are associated with electron-hole (e - h) pairs near E_F in the CB, induced in response to the VB hole created during photoemission. In the undoped situation sketched in Fig. 4(a) such interactions are not possible. At high carrier densities where the CB is occupied an e - h excitation around \bar{K} (or \bar{K}') can interact with the VB photohole, forming a positively charged, bound electron-hole-hole complex denoted as $e_c h_c h_v$, where (c, v) denotes charges in the (CB, VB), respectively, as illustrated in Fig. 4(b). Such a process would renormalize the bare band dispersion and lifetime of the VB states, broadening and shifting their spectra as observed.

These excitations may be compared to the X^+ (X^-) trions found in p - (n)-doped TMDs with configuration $e_c h_v h_v$ ($e_c e_c h_v$). Such trions have been invoked to interpret additional spectral lines shifted in energy by ~ 20 -60 meV with respect to the main A exciton line in optical absorption [6] and luminescence [6, 29] measurements of SL TMDs. Our measurements show a relative shift of VB_A by ~ 0.23 eV compared to VB_B , which reflects the absolute binding energy reduction ΔE_{ehh} of the photohole associated with the formation of the trion (see Fig. 4(b)). The order of magnitude of ΔE_{ehh} is compatible with the absolute trion binding energies that can be extracted from the optical experiments [6, 29], however, the exact values are expected to depend on the dielectric environment of the sample and the doping. So far, corresponding trion features associated with B excitons have not been observed in optical experiments, which is fully consistent with the absence of renormalization of the VB_B dispersion in the present ARPES data, as seen in Figs. 3(a)-(e) and as sketched in Fig. 4(c). This lack of renormalization of the VB_B dispersion might be attributed to additional decay channels of the VB_B hole such as decay into the VB_A band. The dramatic increase of Δ_{SO} and the band gap renormalization can therefore be viewed as direct consequences of forming trionic quasiparticles around the VB_A and CB extrema.

The assignment of trions in optical measurements of semiconducting TMDs is currently being debated, as a recent theoretical study points towards the possibility of interactions between e - h pairs and the remaining charge density forming other types of quasiparticles such as exciton-polarons [30]. Our ARPES measurements provide direct evidence for such multi-component excitations in SL TMDs and gives access to both their energy and momen-

tum dependence that is lacking from momentum-integrating transport, optical, or tunneling measurements. We envision further theoretical and experimental studies to disentangle such many-body effects in the spectral function of SL TMDs. The charge carrier dependent electronic band gap and spin-splitting that arise from these many-body effects will profoundly impact the charge-, spin- and valley-dependent dynamics and transport properties of devices, as well as the interpretation of excitonic effects.

METHODS

Fabrication of WS₂/h-BN heterostructures. The heterostructures were prepared by successively transferring few layer h-BN (commercial crystal from HQ Graphene) and then SL WS₂ onto 0.5 wt % Nb-doped rutile TiO₂(100) purchased from Shinkosha Co., Ltd. A thin film of polycarbonate (PC) was mounted onto polydimethylsiloxane (PDMS) on a glass slide to prepare a PC/PDMS stamp. This stamp was first utilized to pick up h-BN flakes from a SiO₂ substrate and then dropped onto the TiO₂ substrate under a microscope. The transferred h-BN flakes were cleaned of any polymer residue by annealing at 625 K in UHV for 1 hour. Next, SL WS₂ flakes were picked up from the SiO₂ growth substrate and aligned to drop onto h-BN, such that a part of the flake makes contact with the TiO₂ substrate. The process is followed by another annealing step in UHV to clean of any remaining residues.

microARPES experimental details. The samples were transported through air to the Microscopic and Electronic Structure Observatory (MAESTRO) at the Advanced Light Source (ALS) where they were inserted in the microARPES UHV end-station with a base pressure better than 5×10^{-11} mbar. The samples were given a mild anneal at 600 K prior to measurements in order to desorb adsorbates from air. The synchrotron beam-spot size was on the order of 10 μm for the photon energies of 145 eV and 76.5 eV used to obtain the microARPES data. The data were collected using a hemispherical Scienta R4000 electron analyzer equipped with custom-made deflectors that enable collecting ARPES spectra over a full BZ without moving the sample. Potassium dosing experiments were carried out *in situ* using SAES getters mounted in the analysis chamber such that dosing could be completed on an optimum sample position without ever moving the sample. Core level data of undoped and potassium dosed samples are presented in Supplementary Figure S2 to document the cleanliness of the samples. The data in Figs. 1-2 are from the same sample,

while the data in Fig. 3 and Supplementary Figure S8 were obtained on fresh samples. The charge carrier density N is estimated using a simple model of a 2D parabolic band given by $N = (g_v g_s m_{cb}^* k_B T / 2\pi \hbar^2) \ln(1 + e^{E - E_F / k_B T})$, where the factors $g_v = 2$ and $g_s = 2$ take spin- and valley-degeneracy into account, m_{cb}^* is the effective mass of the SL WS₂ CB obtained from Ref. [12], k_B is Boltzmann's constant, \hbar is the reduced Planck constant, T is the sample temperature and $E - E_F$ is determined from the fitted CBM position. The total energy and momentum resolution in the microARPES data were better than 20 meV and 0.01 Å⁻¹, respectively. Measurements and dosing experiments were carried out at both 85 K and at 20 K, without any noticeable change in behavior between the two temperatures.

Data availability. The data that support the plots within this paper and other findings of this study are available from the corresponding author upon reasonable request.

ACKNOWLEDGEMENT

We thank Allan H. MacDonald for helpful discussions. S. U. acknowledges financial support from the Danish Council for Independent Research, Natural Sciences under the Sapere Aude program (Grant No. DFF-4090-00125) and from VILLUM FONDEN (Grant. No. 15375). R. J. K. is supported by a fellowship within the Postdoc-Program of the German Academic Exchange Service (DAAD). S. M. acknowledges support by the Swiss National Science Foundation (Grant No. P2ELP2-155357). The Advanced Light Source is supported by the Director, Office of Science, Office of Basic Energy Sciences, of the U.S. Department of Energy under Contract No. DE-AC02-05CH11231. This work was supported by IBS-R009-D1. The work at Ohio State was primarily supported by NSF-MRSEC (Grant DMR-1420451). Work at NRL was supported by core programs and the NRL Nanoscience Institute, and by AFOSR under contract number AOARD 14IOA018- 134141.

AUTHOR CONTRIBUTIONS

J. K. and S. U. conceived and planned the experiments. K. M. M. and B. T. J. synthesized the SL WS₂ flakes on SiO₂. J. K., S. S., J. X. and R. K. K assembled the WS₂/h-BN heterostructures on TiO₂. S. U., R. J. K., S. M., J. K., A. B., E. R. and C. J. performed the microARPES experiments. The microARPES setup was developed and maintained by

C. J., A. B. and E. R.. S. U. analyzed the experimental data with inputs from C. J. and E. R.. All authors contributed to the interpretation and writing of the manuscript.

AUTHOR INFORMATION

The authors declare that they have no competing financial interests. Supplementary Information accompanies this paper. Correspondence and requests for materials should be addressed to C.J. (CMJozwiak@lbl.gov)

-
- [1] A. Chernikov, A. Zande, H. Hill, A. Rigosi, A. Velauthapillai, J. Hone, and T. Heinz, *Physical Review Letters* **115**, 126802 (2015).
 - [2] Y. Liang and L. Yang, *Physical Review Letters* **114**, 063001 (2015).
 - [3] A. Chernikov, C. Ruppert, H. Hill, A. Rigosi, and T. Heinz, *Nature Photonics* **9**, 466 (2015).
 - [4] A. Ramasubramaniam, *Physical Review B* **86**, 115409 (2012).
 - [5] D. Qiu, F. Jornada, and S. Louie, *Physical Review Letters* **111**, 216805 (2013).
 - [6] K. F. Mak, K. He, C. Lee, G. H. Lee, J. Hone, T. F. Heinz, and J. Shan, *Nature Materials* **12**, 207 (2013).
 - [7] D. Xiao, G. Liu, W. Feng, X. Xu, and W. Yao, *Physical Review Letters* **108**, 196802 (2012).
 - [8] A. Geim and I. Grigorieva, *Nature* **499**, 419 (2013).
 - [9] M. Ugeda, A. Bradley, S. Shi, F. Jornada, Y. Zhang, D. Qiu, W. Ruan, S. Mo, Z. Hussain, Z. Shen, et al., *Nature Materials* **13**, 1091 (2014).
 - [10] S. Larentis, J. R. Tolsma, B. Fallahazad, D. C. Dillen, K. Kim, A. H. MacDonald, and E. Tutuc, *Nano Letters* **14**, 2039 (2014).
 - [11] X. Xu, W. Yao, D. Xiao, and T. Heinz, *Nature Physics* **10**, 343 (2014).
 - [12] A. Kormányos, G. Burkard, M. Gmitra, J. Fabian, V. Zólyomi, N. Drummond, and V. Falko, *2D Materials* **2**, 049501 (2015).
 - [13] K. F. Mak and J. Shan, *Nature Photonics* **10**, 216 (2016).
 - [14] Y. Ferreira and A. Cortijo, *Physical Review B* **90**, 195426 (2014).
 - [15] A. Bostwick, T. Ohta, T. Seyller, K. Horn, and E. Rotenberg, *Nature Physics* **3**, 36 (2007).
 - [16] Y. Zhang, T. Chang, B. Zhou, Y. Cui, H. Yan, Z. Liu, F. Schmitt, J. Lee, R. Moore, Y. Chen,

- et al., *Nature Nanotechnology* **9**, 111 (2014).
- [17] Y. Zhang, M. Ugeda, C. Jin, S. Shi, A. Bradley, M. Ana, H. Ryu, J. Kim, S. Tang, Y. Kim, et al., *Nano Letters* **16**, 2485 (2016).
 - [18] J. Miwa, S. Ulstrup, S. Sørensen, M. Dendzik, A. G. Čabo, M. Bianchi, J. Lauritsen, and P. Hofmann, *Physical Review Letters* **114**, 046802 (2015).
 - [19] W. Jin, P. Yeh, N. Zaki, D. Zhang, J. Sadowski, A. Abdullah, A. Zande, D. Chenet, J. Dadap, I. Herman, et al., *Physical Review Letters* **111**, 106801 (2013).
 - [20] C. Dean, A. Young, I. Meric, C. Lee, L. Wang, S. Sorgenfrei, K. Watanabe, T. Taniguchi, P. Kim, K. Shepard, et al., *Nature Nanotechnology* **5**, 722 (2010).
 - [21] L. Wang, I. Meric, P. Huang, Q. Gao, Y. Gao, H. Tran, T. Taniguchi, K. Watanabe, L. Campos, D. Muller, et al., *Science* **342**, 614 (2013).
 - [22] E. Wang, X. Lu, S. Ding, W. Yao, M. Yan, G. Wan, K. Deng, S. Wang, G. Chen, L. Ma, et al., *Nature Physics* **12**, 1111 (2016).
 - [23] S. Ulstrup, J. Katoch, R. Koch, D. Schwarz, S. Singh, K. McCreary, H. Yoo, J. Xu, B. Jonker, R. Kawakami, et al., *ACS Nano* **10**, 10058 (2016).
 - [24] M. Dendzik, M. Michiardi, C. Sanders, M. Bianchi, J. Miwa, S. Grønborg, J. Lauritsen, A. Bruix, B. Hammer, and P. Hofmann, *Physical Review B* **92**, 245442 (2015).
 - [25] J. Riley, W. Meevasana, L. Bawden, M. Asakawa, T. Takayama, T. Eknapakul, T. Kim, M. Hoesch, S. Mo, H. Takagi, et al., *Nature Nanotechnology* **10**, 1043 (2015).
 - [26] H. Yuan, M. Bahramy, K. Morimoto, S. Wu, K. Nomura, B. Yang, H. Shimotani, R. Suzuki, M. Toh, C. Kloc, et al., *Nature Physics* **9**, 563 (2013).
 - [27] K. V. Shanavas and S. Satpathy, *Physical Review B* **91**, 235145 (2015).
 - [28] M. Kang, B. Kim, S. H. Ryu, S. W. Jung, J. Kim, L. Moreschini, C. Jozwiak, E. Rotenberg, A. Bostwick, and K. S. Kim, *Nano Letters* **17**, 1610 (2017).
 - [29] B. Zhu, X. Chen, and X. Cui, *Scientific Reports* **5**, 9218 (2015).
 - [30] D. K. Efimkin, and A. H. MacDonald, *Physical Review B* **95**, 035417 (2017).